

## Velocity field measurements under Very Large Floating Structures interacting with surface waves

Uksul, Esra; Laskari, Angeliki; Schreier, Sebastian; Poelma, Christian

**DOI**

[10.1016/j.oceaneng.2024.119759](https://doi.org/10.1016/j.oceaneng.2024.119759)

**Publication date**

2025

**Document Version**

Final published version

**Published in**

Ocean Engineering

**Citation (APA)**

Uksul, E., Laskari, A., Schreier, S., & Poelma, C. (2025). Velocity field measurements under Very Large Floating Structures interacting with surface waves. *Ocean Engineering*, 315, Article 119759. <https://doi.org/10.1016/j.oceaneng.2024.119759>

**Important note**

To cite this publication, please use the final published version (if applicable). Please check the document version above.

**Copyright**

Other than for strictly personal use, it is not permitted to download, forward or distribute the text or part of it, without the consent of the author(s) and/or copyright holder(s), unless the work is under an open content license such as Creative Commons.

**Takedown policy**

Please contact us and provide details if you believe this document breaches copyrights. We will remove access to the work immediately and investigate your claim.



## Research paper

# Velocity field measurements under Very Large Floating Structures interacting with surface waves

Esra Uksul<sup>a,\*</sup>, Angeliki Laskari<sup>a</sup>, Sebastian Schreier<sup>b</sup>, Christian Poelma<sup>a</sup>

<sup>a</sup> Process and Energy, Faculty of Mechanical Engineering, Delft University of Technology, Delft, The Netherlands

<sup>b</sup> Maritime and Transport Technology, Faculty of Mechanical Engineering, Delft University of Technology, Delft, The Netherlands

## ARTICLE INFO

## Keywords:

Very Large Floating Structure (VLFS)  
Fluid–structure interactions  
Wave attenuation  
Wave boundary layer  
Characteristic length

## ABSTRACT

Increasing utilization of ocean space and a global push for renewable energy solutions has spurred interest in wave behavior around Very Large Floating Structures, like floating photovoltaic (PV) systems. Flexible PV modules may be more suitable for the varying wave conditions found in offshore environments. However, while viscoelastic models are commonly used for wave prediction, they show notable discrepancies with experiments, likely due to untested assumptions of inviscid flow. This experimental study aims to fill that gap by investigating both the wave characteristics and velocity fields underneath flexible and rigid structures using simultaneous Particle Image Velocimetry (PIV) and wave elevation measurements. Wave attenuation is observed for short wavelengths over the flexible structure length. The 2nd order Stokes wave theory provides a good approximation of the wave-induced horizontal velocity profiles under the flexible structure but underestimates the velocities under the rigid one which further lacks the typical exponential decay with water depth. The presence of a wave boundary layer is showcased and compared to an adaptation of the Stokes 2nd problem.

## 1. Introduction

An effective approach for mitigating the rising demand for developable space, particularly in densely populated coastal regions, involves expanding onto adjacent bodies of water. One promising solution to address the challenges linked with land scarcity is presented by Very Large Floating Structures (VLFS). A particular application of VLFS that has garnered increased attention stems from the pressing need to cultivate more sustainable and carbon-free energy sources: floating photovoltaics (PV) (Sahu et al., 2016). These floating PV systems can be strategically deployed across both inland water bodies and offshore locations (Fig. 1). To date, the predominant deployment of floating PV systems has taken place on inland water bodies, such as lakes or reservoirs. The offshore floating PV technology application is still in its initial phase, primarily due to the harsh ocean conditions they must withstand (Zhang and Schreier, 2022). Nonetheless, the potential of exploiting the vast oceanic space, especially for renewable technologies makes them a compelling prospect for exploration. To effectively implement them on large scales, flexible VLFS might be more advantageous than rigid ones in the dynamic ocean environment; however, predicting their behavior is much more complex.

## 1.1. Very large floating structures

VLFS possess two distinctive characteristics: a substantial length  $L$  to height  $H_t$  ratio and a low bending rigidity, resulting in hydroelastic responses dominating over rigid body motion (Wang and Tay, 2011). The assessment of flexibility on structural responses can be quantified through a characteristic length  $\lambda_c$  (Suzuki et al., 2007):

$$\lambda_c = 2\pi \left( \frac{EI}{k_c} \right)^{\frac{1}{4}} \quad (1)$$

where  $EI$  is the bending stiffness of a beam,  $k_c = \rho g B$  the spring constant of the hydrostatic restoring force,  $\rho$  the fluid density and  $B$  the width of the structure.  $\lambda_c$  represents the length of a structure over which the effects of a concentrated load are felt: for  $\lambda_c > L$  rigid body motion is dominant (Fig. 2). Conversely, for flexible bodies,  $\lambda_c$  is smaller than the overall structural length, so the effects of an applied load are constrained to a smaller region of the structure, resulting in more localized deformations. Local deformations refer to alterations in the form or sizing of a structure that develops in a limited region rather than uniformly across the entire structure. These deformations are usually an effect of concentrated stresses, causing certain regions to sustain modifications in response to applied loads. In the context of

\* Corresponding author.

E-mail address: [e.uksul@tudelft.nl](mailto:e.uksul@tudelft.nl) (E. Uksul).



Fig. 1. (Left) 39 MW floating solar project in Xiangshan, Zhejiang, China (reprinted, with permission, from Chen and Zhou (2023) © Elsevier), (right) the North Sea hosts the world's first offshore solar farm modules at open sea (reprinted, with permission, from Oceans of Energy (2024)).

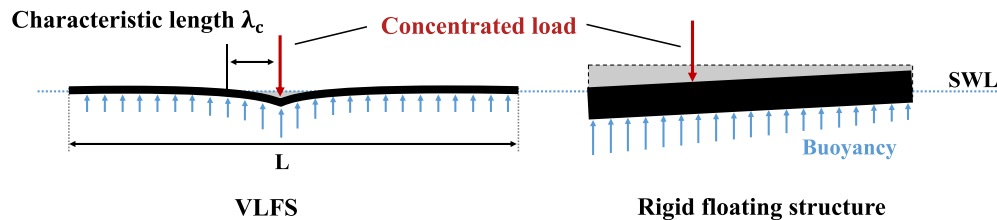


Fig. 2. Global response of a VLFS and a rigid floating structure under a static load.  
Source: Adapted from Suzuki et al. (2007).

VLFS, where flexibility is a notable feature,  $\lambda_c$  helps differentiate the behavior of these structures from rigid ones under concentrated loads.

The exploration of floating thin elastic structures also holds relevance in the context of sea ice dynamics. This relates to the analysis of wave propagation through the transition region between open water and sea ice cover in polar oceans, known as the marginal ice zone. Notable modeling resemblances emerge in the interaction of waves with VLFS and sea ice, with both fields recognizing the scarcity of experimental data to substantiate the expanding realm of theoretical research (Squire, 2007; Chen et al., 2006).

Considerable attention has been directed towards understanding the behavior of ocean waves propagating through articulated VLFS models (Bispo et al., 2022, 2023) and ice-covered waters (Wadhams et al., 1988; Wang and Shen, 2010) since this occurrence has been associated with mechanisms such as wave attenuation, scattering, and viscous damping (Mosig et al., 2015). Several theoretical studies and models explore the viscoelastic responses of floating ice covers, which are relevant to interactions of waves and continuous flexible covers (Hermans, 2004; Mosig et al., 2015). In a flume setting, Sree et al. (2018) performed experiments with oil-doped Polydimethylsiloxane (PDMS) sheets of varying viscoelastic qualities and structure thicknesses in low amplitude surface waves. Comparisons were made between the observed wave attenuation, shifts in wavelength and wave speed under the viscoelastic structure, and the prevalent viscoelastic models for sea ice, as described in Squire (2007), Robinson and Palmer (1990) and Wang and Tay (2011). The wave propagating underneath the flexible floating structure displayed changes based on wave and material properties, with wave shortening observed for viscoelastic PDMS covers across all wave periods, and wavelength elongation observed for stiffer sheets, mirroring earlier findings (Sree et al., 2017). The viscoelastic models correlated well with the experimental results for thinner structures and larger wave periods, while discrepancies emerged, particularly in terms of wave attenuation, for shorter wave periods and larger cover thicknesses. Similarly, Sutherland et al. (2017) found that the stiffer and thicker structures had larger errors compared to the exponential wave attenuation fits, likely due to the inexact surface tracking compared to the thinner and more membrane-like structures.

Sree et al. (2018) attributed the divergence between viscoelastic models and experimental outcomes to viscous dissipation within an

oscillating, potentially turbulent boundary layer beneath the floating flexible structure. Although the influence of boundary layers can be minor for relatively rigid structures, as commonly seen in most VLFS, their impact on local structural deformation can be considerable for highly flexible structures, as demonstrated in cases such as Wang et al. (2020).

To the authors' knowledge, only two experiments to date have measured the velocity field underneath a flexible structure in waves. The first one was a wave tank experimental campaign by Rabault et al. (2019), on the dynamics of discontinuous ice cover/grease ice in waves. Concurrent wave elevation and Particle Image Velocimetry (PIV) for the water velocity were performed. Through this analysis, it was discovered that a dynamic vortex forms beneath the ice layer as segments of ice collide under the influence of wave-induced forces. More recently, Orzech et al. (2022) undertook measurements in a saltwater tank where waves interacted with ice floes. They employed a submerged PIV system to visualize the wave kinematics at the interface between the discontinuous ice and water. The observed wave attenuation aligned with findings from previous laboratory experiments documented in the literature. Furthermore, the flow visualization revealed evidence of a boundary layer at the ice-water interface. Both studies provided initial insights into the wave-ice boundary layer formation under discontinuous sheets. Under floating ice floes, wave propagation is primarily influenced by the irregular surface of the ice and the collisions of fragmented ice pieces due to their in-plane mobility. However, in the case of a continuous, uniformly viscoelastic structure, as seen in studies such as Sree et al. (2018) or Schreier and Jacobi (2021) wave dynamics at the fluid-structure interface depend primarily on the flexural rigidity of the structure and the viscosity of the fluid.

The goal of this experimental study was to advance our understanding of VLFS by directly examining wave characteristics and velocity fields of regular waves propagating under continuous structures of different stiffness. We investigated both very flexible and rigid structures using techniques that simultaneously measure wave elevation and flow visualization. Theoretical solutions are compared with experimental data to assess the impact of these structures, with particular attention to the potential presence of a wave boundary layer (WBL).

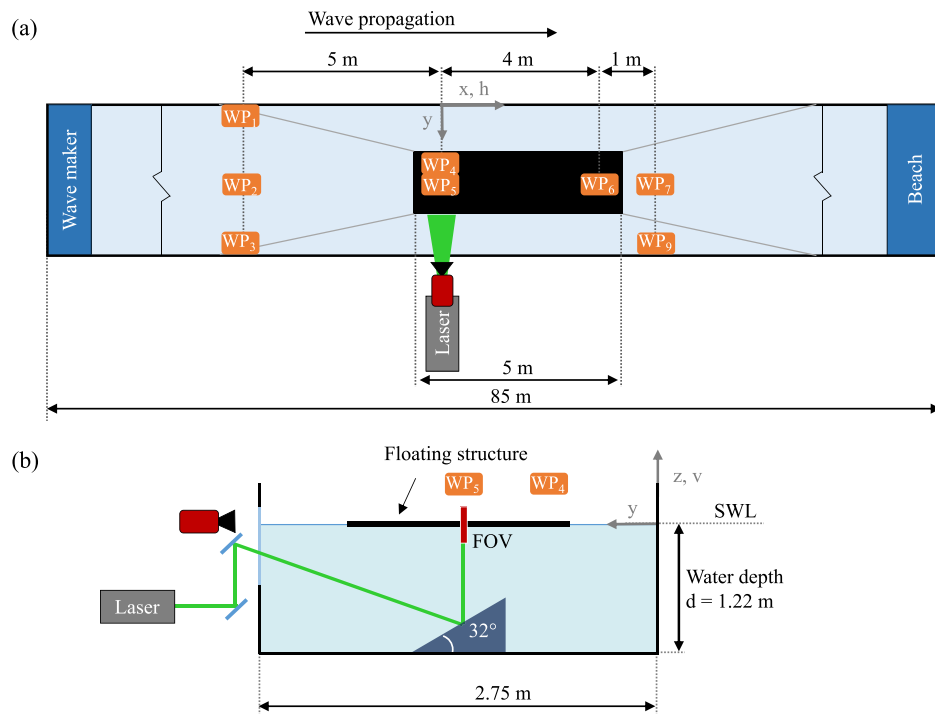


Fig. 3. Schematic of wave tank and experimental setup: top view (a) and cross section (b).

## 2. Experiments

### 2.1. Setup

The experiments were conducted in towing tank No. 2 of the Department of Maritime and Transport Technology at TU Delft. The tank spans 85 m in length and 2.75 m in width, while the depth of the water  $d$  was 1.22 m during the measurement campaign. The water temperature was 20.5 °C. Situated at one end of the tank is a piston/flap-type wave maker used in piston mode, and at the opposite end lies a damping beach (Fig. 3).

Planar PIV measurements, made possible by optical access through the side window of the tank, were conducted in the  $x$ - $z$  plane. Simultaneously, wave elevation measurements were conducted using probes at various positions in the  $x$ - $y$  plane. Two test structures were studied: a very flexible floating cover and a rigid floating structure.

Details of the PIV system parameters and equipment are shown in Table 1. A double-pulse laser was used for PIV illumination. The laser beam (3 mm) was expanded into a sheet and guided with mirrors towards illuminating the midplane of the structure. The PIV camera had a field of view (FOV) of  $12 \times 15 \text{ cm}^2$  at the center plane of the tank with a resolution of 17 pixel/mm (magnification  $M = 0.11$ ). The system was synchronized through a LaVision (Göttingen, Germany) PTU controller in conjunction with Davis 10 software. For synchronization with the wave phase, an Arduino Micro was used. The water was seeded with neutrally buoyant  $10 \mu\text{m}$  diameter hollow glass spheres (Spherical, Potters Industries) and treated with a surfactant (Tween) to mitigate particle clustering (Westerweel, 1997).

Eight wave probes, comprising four acoustic (WP<sub>2</sub>, WP<sub>4</sub>, WP<sub>5</sub>, WP<sub>6</sub>) and four wired, resistance-based (WP<sub>1</sub>, WP<sub>3</sub>, WP<sub>7</sub>, WP<sub>8</sub>), were strategically placed throughout the tank (Fig. 3). WP<sub>2</sub>, positioned midplane of the tank, served as both a wave probe and a camera trigger, which will be discussed later. The wired, resistance-type wave probes (in-house built) were calibrated each day, in steps of 10 mm over a range of 200 mm. Notably, maximum errors were most pronounced at the sensor range extremities, with the largest discrepancy being 2.8% in the measurement range. The acoustic wave probes (General Acoustics, Kiel,

Table 1

Summary of the PIV system parameters.

Laser	Litron Bernoulli Nd: YAG	
	Wavelength	532 nm
	Output energy per laser	100 mJ
	Max. frequency	50 Hz
Camera	Imager sCMOS CLHS	
	Resolution	$2560 \times 2160$ pixels
	Pixel pitch	$6.5 \mu\text{m}$
	Image rate	25 Hz
Lens	Nikon Macro Lens	
	Focal length	200 mm
	Aperture	$f/4$

Germany) have a measuring range spanning 200–1200 mm, a maximum sample rate of 100 Hz, an accuracy of 1 mm, and a resolution of 0.18 mm. These wave probes self-calibrate through an additional probe that continuously measures the speed of sound with an accuracy of 0.1  $\text{m s}^{-1}$ . Due to the fact that acoustic wave probes are also non-invasive, they complement simultaneous PIV measurements well and have been shown to have higher resolution and better accuracy than more traditional wave probes like resistive, capacitive, or servo-mechanical probes (Bouvy, 2009).

### 2.2. Test structures

The flexible structure has a length  $L = 5 \text{ m}$ , width  $B = 1.02 \text{ m}$  and thickness  $H_t = 0.0048 \text{ m}$ . It is made from closed-pore neoprene foam with a density of  $145.42 \text{ kg m}^{-3}$  and  $\lambda_c = 0.193 \text{ m}$  with Young's modulus  $E = 828 \text{ kPa}$  (Fig. 4). The structure stiffness was measured as described in Schreier and Jacobi (2021). The rigid structure needed to be assembled first (Fig. 4). As the building material, closed cell, thermoplastic EPS foam blocks with a density of  $28 \text{ kg m}^{-3}$  were chosen. EPS blocks of  $1 \times 0.6 \times 0.125 \text{ m}^3$  were milled and adhered to the size of  $L = 5 \text{ m}$ ,  $B = 1 \text{ m}$  and  $H_t = 0.125 \text{ m}$ . To maintain similar surface conditions, a layer of neoprene foam was glued onto the assembled EPS structure.



Fig. 4. Floating structures moored in the towing tank facility, (left) flexible and (right) rigid structure.

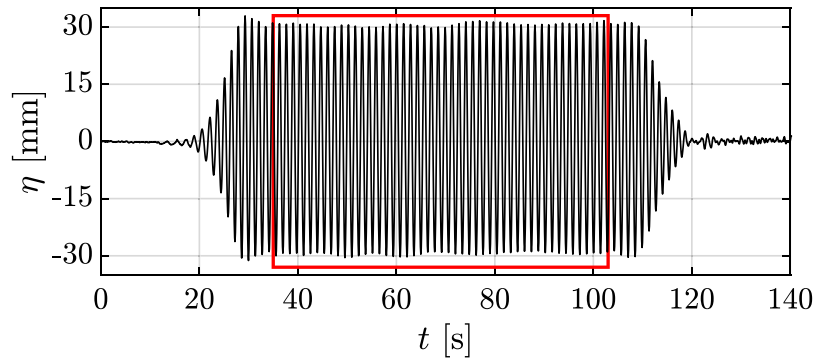


Fig. 5. Measured wave train of W3-2 at WP<sub>2</sub>. The red box indicates the steady state phase of the wave.

Table 2

Wave conditions.  $a$  refers to the wave amplitude and  $\Delta t$  to the time between PIV double images.

Case	$T$ [s]	$\lambda$ [m]	$L/\lambda$	$a$ [m]	$\Delta t$ [ $\mu$ s]	Frame rate [Hz]
W3-1	1.4	3.02	1.66	0.009	13 237	25
W3-2	1.4	3.02	1.66	0.03	4426	25
W6-1	0.65	0.66	7.58	0.011	6160	25
W6-2	0.65	0.66	7.58	0.017	2816	25

To enforce the structure's stiffness, aluminum profiles, and lead weights were placed on top of the structure. The final weight was 241.36 kg. Taking into account the bending stiffness of the two primary aluminum profiles positioned on the EPS foam yields a result of  $\lambda_c = 24.8$  m.

To keep the structures in place even under wave forcing, they were secured by four mooring lines, each 5 m in length, connecting the outer edges of the structure to the tank walls at still water level (SWL). For the front mooring lines, Dyneema lines of 0.2 mm diameter with high stiffness were utilized. At the back of the structure, pre-stretched elastic sewing threads with a 0.5 mm diameter were used with a pretension of 0.208 N.

### 2.3. Data acquisition

The flexible and rigid structures were subjected to four wave conditions, detailed in Table 2. To ensure the reproducibility of the results, each wave condition was tested three times for each structure type. Within each test scenario, we generated wave sequences that span 60 to 80 wave periods  $T$ . We adjusted the duration of each wave train based on the wavelength ( $\lambda$ ) and the wave group speed  $v_g$  to minimize the impact of beach reflections.

With the structure in place and still water conditions, wave generation, and consequent data acquisition began for wave probes. Waves started with a ramp-up phase, continued for 60–80 waves, and then ramped down, see Fig. 5. Here the wave elevation  $\eta$ , measured at

WP<sub>2</sub>, is plotted against recording time  $t$ . Recording of PIV images began once a trigger signal from WP<sub>2</sub> was received, capturing 30–40 wave periods for the performed wave conditions during the waves' steady state phase. After each test run, a minimum of a 30-min waiting period was adhered to allow the water to settle before the subsequent measurement. The phase-locked PIV trigger mechanism sets a threshold on the rising flank of the wave, which originates from WP<sub>2</sub>. This trigger signal is then transmitted by an Arduino to initiate a TTL signal sent to the PIV PTU, thereby starting the PIV recording process. The acquisition details for each wave condition are listed in Table 2. To synchronize the wave probes and the PIV system, the shutter signal from the laser was recorded alongside the wave elevation data. Both, shutter signal and wave probe signals were fed through a low-pass filter with a cut-off frequency of 100 Hz and after that recorded at 1000 Hz.

### 2.4. PIV data processing

Ensemble averaged velocities were obtained by averaging the instantaneous velocity fields for each measured wave phase. The utilization of ensemble averaging is particularly relevant in scenarios involving flows characterized by low seeding density (Santiago et al., 1998). For each wave condition 25 (for  $\lambda = 3.03$  m) or 35 (for  $\lambda = 0.66$  m) waves were measured. Each individual wave is covered by image pairs of 35 or 17, providing full wave coverage. Spatial overlap between consecutive image pairs was low for waves with  $\lambda = 3.03$  m ( $\sim 5\%$ ), and almost 55% for  $\lambda = 0.66$  m. Each image pair, or wave phase, was averaged across the 25 or 35 recorded waves. This quantity proved to be sufficiently large to ensure the convergence of first-order statistics, with variations remaining within the range of  $\pm 5\%$  for averaged values after 25 waves. The resulting velocity fields of consecutive wave phases were stitched together where they overlap and are presented over half of the wavelength for the wave condition W3-2 in Fig. 6. Here, the mean velocity is  $V = \sqrt{U_V^2 + U_H^2}$ , with  $U_V$  being the vertical and  $U_H$  the horizontal velocity. The evaluation of velocity fields was performed using PIV image analysis software (PIVTEC GmbH,

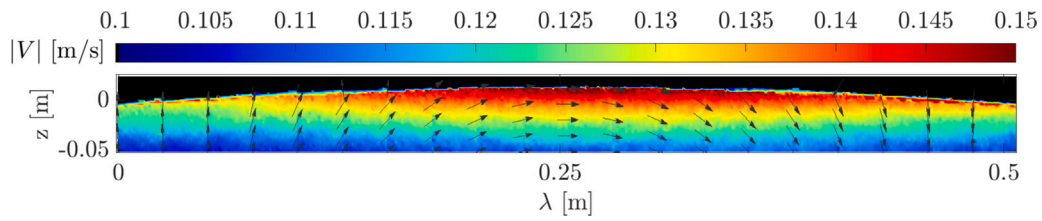


Fig. 6. Phase-averaged velocity profile under the flexible structure of wave W3-2. Here, half of the measured wavelength is displayed and only every 4th vector is shown.

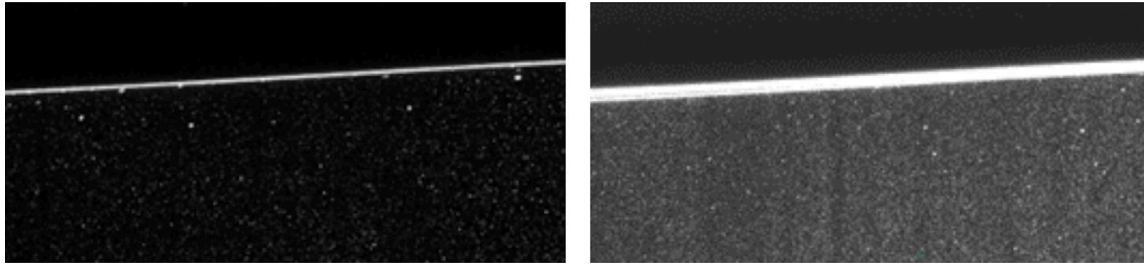


Fig. 7. Section of a raw PIV image (left). Images of the same phase overlaid of wave W3-2.

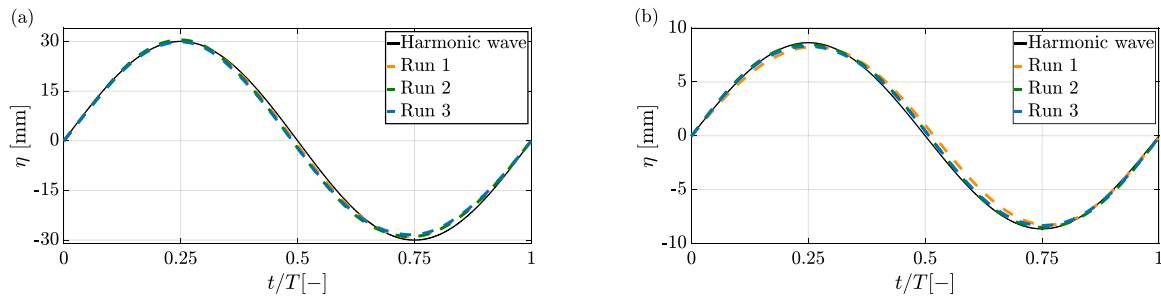


Fig. 8. Deviation between independent runs for  $WP_5$  for wave condition (a) W3-2 and (b) W6-1.

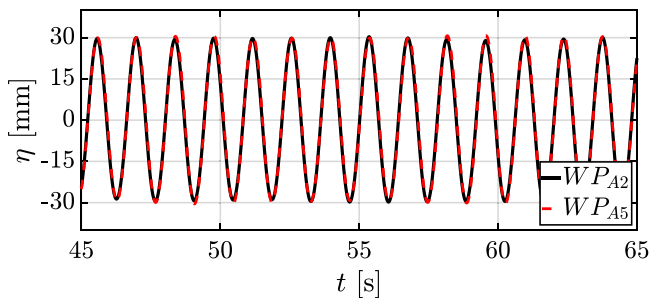


Fig. 9. Wave elevation  $\eta$  of the free surface upstream of the flexible structure ( $WP_2$ ) and above it at the PIV measurement location ( $WP_5$ ).

Göttingen, Germany) with a final interrogation window (IW) size of  $128 \times 128$  pixel, a 50% overlap, resulting in a vector resolution of 3.7 mm.

Commonly, prior to processing of PIV raw images, areas that are not relevant are masked out. In this investigation, we needed to mask regions above the interface between fluid and the structure. Since we are measuring at different wave phases, the mask had to be determined for each phase; for this, we used the partially reflected laser light in order to identify the fluid–structure interface. The structure and the adjacent air above were then manually masked. Within the masked area, intensity levels were set to zero. While theoretically, the generated mask should have been suitable for all 25 images taken at the same wave phase, an overlapping of the raw images exposed a noticeable inconsistency in the position of the illuminated interface (Fig. 7). This

variation band amounted to up to 40 pixel or 2.35 mm. These deviations might be attributed to fluctuations in wave height or inaccuracies in triggering. Heightened uncertainty near the fluid–structure interface is particularly critical when considering a boundary layer. To address this, resulting variations in the theoretical velocity due to a change in either wave elevation or wave phase of magnitude 40 pixel were considered and found to be around 1%. The phased-averaged velocities were subsequently subjected to additional averaging across two IW in the horizontal direction to obtain the velocity profiles under the floating structures.

### 2.5. Wave conditions and theory

The waves under consideration in this study fall within the spectrum of both 2nd (W3-1, W3-2, W6-1) and 3rd order Stokes wave theory (W6-2). In this study, the 2nd order Stokes theory for the wave surface elevation  $\eta$  is considered to compare experimental data with theoretical results. This choice is made under the assumption of intermediate water depth conditions (where  $1/20 \leq d/\lambda \leq 1/2$ ).  $U_{H, Stokes}^{(2)}$  characterizes the horizontal velocity profile throughout the water depth for a 2nd order Stokes wave, as defined below:

$$U_{H, Stokes}^{(2)} = U_{H, Stokes}^{(1)} + \frac{3}{4} \frac{\pi H}{T} \frac{\pi H}{\lambda} \frac{\cosh[2k(z+d)]}{\sinh(kd)^4} \cos 2\theta \quad (2)$$

Here,  $U_{H, Stokes}^{(1)}$  represents the horizontal velocity profile function for the 1st order Stokes wave (Phillips, 1977):

$$U_{H, Stokes}^{(1)}(z, t) = \frac{\pi H}{T} \frac{\cosh[k(z+d)]}{\sinh(kd)} \cos \theta \quad (3)$$

With  $\theta = kx - \omega t$  stands for the phase angle,  $\omega = 2\pi/T$  is the wave circular frequency, and  $k = 2\pi/\lambda$  is the wave number.  $H$  describes the

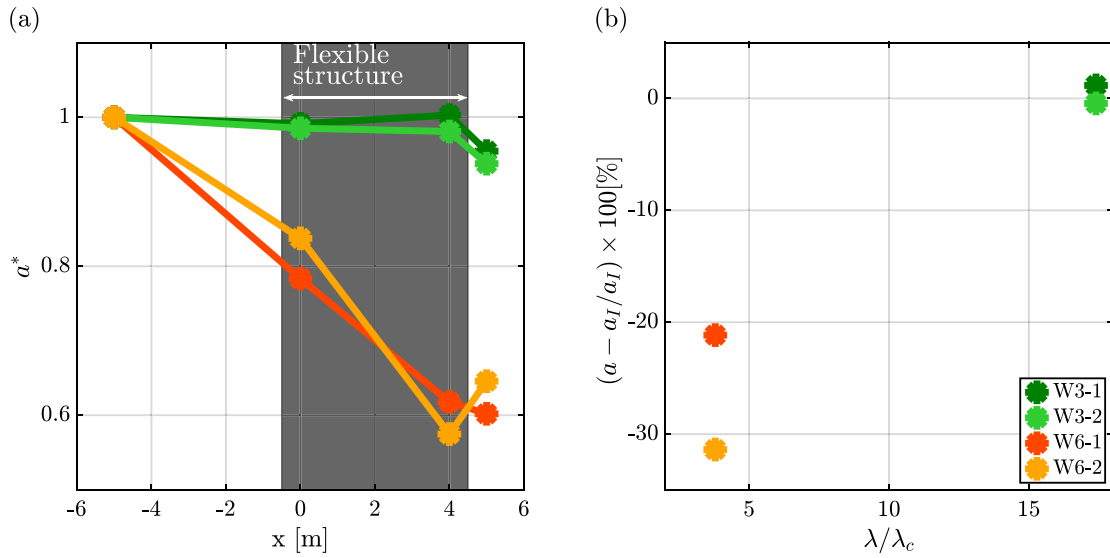


Fig. 10. (a) Wave attenuation for the flexible structure for all different wave cases and (b) resulting wave amplitude reduction.

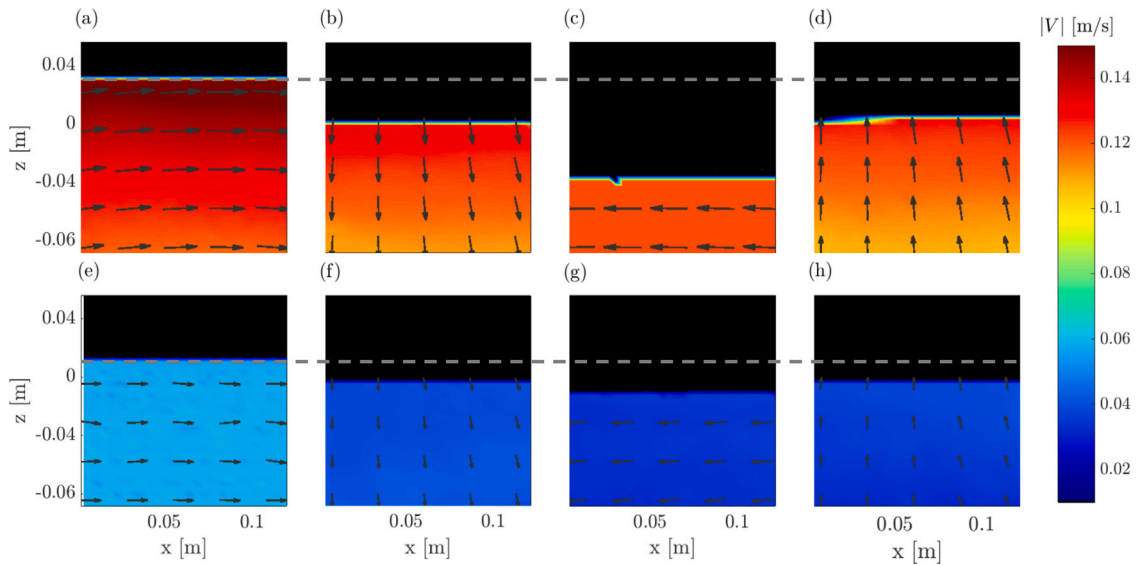


Fig. 11. (Top) phase-averaged velocity fields of W3-2 at different wave phases under the flexible structure. (Bottom) Corresponding wave phases under the rigid structure. The gray dashed lines indicate the measured crest amplitude for each structure. The velocity fields only display every 7th vector.

wave height,  $T$  the wave period. It is worth noting that this analytical solution exclusively applies to the scenario of a free surface wave. In contrast, our study focuses on waves with surface conditions imposed by either compliant or rigid bodies. An analogous benchmark problem closely aligned with our investigation is the Stokes 2nd problem, also known as the Stokes solution for oscillatory boundary layers (Stokes, 1880). This problem describes the flow generated by a rigid plate oscillating in-plane with a velocity  $U(t) = U_0 \cos \theta$ . The solution for the one-dimensional Stokes 2nd problem can be analytically derived by employing the Navier–Stokes equation, the continuity equation, and applicable boundary conditions. This yields a function describing the velocity profile through the fluid depth as a function of  $z$ :

$$\hat{U}(z,t) = U_0 e^{-\sqrt{\frac{\omega}{2\nu}} z} \cos\left(\sqrt{\frac{\omega}{2\nu}} z - \omega t\right) \quad (4)$$

Here,  $U_0$  represents the maximum horizontal velocity of the fluid at the interface,  $\nu$  the kinematic viscosity of the fluid. However, in this study, we consider inverse forcing: a flow that oscillates with  $U_{H, Stokes}^{(2)}$  over a stationary ‘wall’. This is achieved by altering the frame

of reference to follow the wall instead and subtracting Eq. (2) from Eq. (4):

$$U_H^*(z,t) = U_{H, Stokes}^{(2)} - \hat{U}(z,t) \quad (5)$$

A similar modification to Stokes’ 2nd problem is commonly used for sea bottom boundary layer formation under wave and current forcing, e.g. Lorke et al. (2002). Here, we are utilizing this method for WBL for the first time, additionally incorporating the exponential velocity decay from the water surface throughout the water depth. The experimental results will be compared with  $U_{H, Stokes}^{(2)}$  to gauge the influence of the structure and with  $U_H^*$  to consider the boundary layer effects.

### 3. Results and discussion

#### 3.1. Wave probes

Repeatability assesses wave similarity within and between independent test runs, achieved through a minimum of three repetitions of the experimental condition. During the wave’s steady state, each

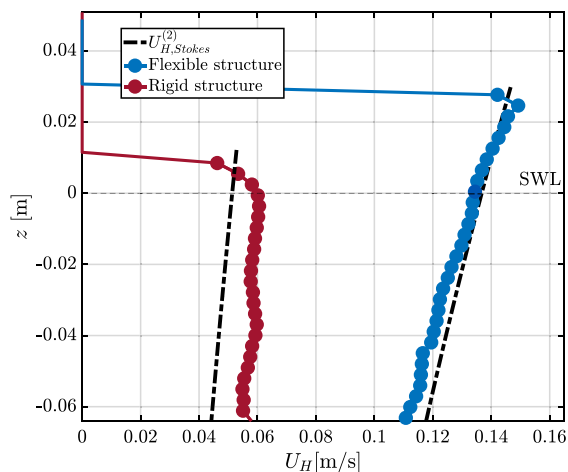


Fig. 12. Results of  $U_H$  distribution across the water column under wave crest between flexible and rigid floating structures for wave W3-2, juxtaposed against theoretical solutions.

wave is divided at every second zero-crossing, and values across the 25 or 35 single wave periods are averaged (Windt et al., 2019). Averaged elevation for waves W3-2 and W6-1 are displayed in Fig. 8, indicating close agreement between independent runs. This repeatability eliminates the need for multiple runs, validating single-run data for further analysis. Notably, wave W3-2 shows better repeatability between independent runs than W6-1, with shorter waves exhibiting larger deviations 1.36%–4.63%.

The study aims to understand how the characteristics of the waves, specifically the amplitude  $a$ , are affected by wave propagation through a floating structure. Here, only the flexible structure will be discussed, as inconsistencies in the structure elevation above the rigid structure did not allow for in-depth analysis. An example of the collected data is depicted in Fig. 9, where surface profiles ( $\eta$ ) are plotted against time with phase lag adjusted. Measurements of the wave probes WP<sub>2</sub> and WP<sub>5</sub> were taken during the interaction of incident wave W3-2 with the flexible structure. The wave elevation above the flexible structure (WP<sub>5</sub>) matches the incoming free surface wave (WP<sub>2</sub>) very well. To determine the wave amplitudes during the steady-state interval at each wave gauge position,  $a = H/2$  was calculated using the vertical distance  $H$  between adjacent wave crests and troughs.

The normalized wave amplitudes  $a^* = a/a_1$ , with  $a$  being the measured and averaged crest amplitude at each location and  $a_1$  being the upstream free surface crest amplitude, are plotted against the distance along the length of the wave tank, which includes the flexible structure for all four waves (Fig. 10(a)). The results show that for longer wavelengths (W3-1, W3-2), the elevation remained relatively consistent across the flexible structure and no significant attenuation occurred. Conversely, the shorter investigated wavelengths, W6-1 and W6-2, demonstrated a notable reduction in wave height when propagating under the flexible structure. Fig. 10 illustrates that amplitude decreases as one moves downstream of the leading edge of the flexible structure. This attenuation tendency is influenced not only by the structure stiffness (Sutherland et al., 2017) and wavelength but also by the wave height, as demonstrated by W6-2, which exhibited relatively higher attenuation levels compared to W6-1. Waves with shorter wavelengths or higher wave frequencies are known to experience greater wave attenuation, a phenomenon well documented in the existing literature (Sree et al., 2018; Sutherland et al., 2017; Schreier and Jacobi, 2022).

The ratios between  $L/\lambda$  and  $\lambda/\lambda_c$  seem to be important indications for wave attenuation. Here, in the case of W3-1 and W3-2, where the ratio  $L/\lambda$  is 1.6, compared to a ratio of 8.33 for W6-1 and W6-2, there are over five times as many shorter waves distributed along

the length of the structure. This increased density of shorter waves allows for a longer duration of fluid–structure interactions.  $\lambda/\lambda_c$ , which represents the ratio of wavelength to the structure’s characteristic length (Fig. 10(b)) provides insights into the importance of structural stiffness under specific wave conditions. A smaller  $\lambda/\lambda_c$  signifies a more significant global response or suggests that the structure appears stiffer from a hydrodynamic perspective (Zhang and Schreier, 2022).

### 3.2. PIV measurements

Fig. 11 showcases the ensemble phase-averaged velocity fields that correspond to four characteristic wave phases for the W3-2 wave condition, observed under both flexible and rigid structures respectively. Waves propagate from right to left. These phases include: (a, e) the wave crest, (b, f) the zero down-crossing, (c, g) the wave trough, and (d, h) the zero up-crossing. When the wave elevation leads to a descent beyond SWL or  $z = 0$ , the point where this descent occurs is termed the zero-down crossing point. Conversely, the zero-up crossing point of a wave is the opposite, i.e. the wave elevation goes up. The crest of a wave was defined as the point on the wave’s profile where it reaches its global maximum amplitude between a zero up-crossing and the subsequent zero down-crossing. Similarly, the trough of a wave can be defined in the corresponding manner.

The depicted vector fields portray a velocity distribution akin to that of free surface regular waves. In particular, maximum velocities manifest near the wave-structure interface and gradually decrease with  $z \rightarrow -d$ . Fluid movement aligns with the wave’s direction beneath the crest, while under the trough, the fluid’s movement counters it. The initial wave condition presented here is characterized by moderate steepness and while the influence of the flexible structure might not be immediately apparent from the vector fields alone, the influence of the rigid structure on the same incident wave is apparent in comparison.

When comparing the four phases of W3-2 as it propagates under both flexible and rigid structure, a noticeable decrease in wave elevation becomes evident. By examining the wave elevation data collected simultaneously just above the PIV measurement area, we observe distinct variations in amplitude between the two structures at the wave crest and trough (Fig. 11): specifically, a difference of 18.5 mm between the crests (a, e) and 21.4 mm at the trough (c, g). The comparison also shows an apparent correlation between the elevation of the interface and the magnitude of the velocity below.

Both flexible and rigid structures also exhibit an asymmetry of amplitude in crest and trough. The wave crest maintains an average amplitude  $a$  of 30 mm (Fig. 11, (a)) (11.5 mm under the rigid structure (b)), while the trough amplitude is around 28 mm only (c) (6.5 mm under the rigid structure (g)).

To comprehensively understand the impact of the floating structures on wave kinematics, it is crucial to draw parallels between experimental data and theoretical concepts concerning free surface waves. Illustrated in Fig. 12 is the horizontal velocity  $U_H$  at the wave crest for W3-2 under both the flexible and rigid structure plotted against the water depth  $z$ . The theoretical solution is incorporated for a free surface 2nd order Stokes wave in intermittent water depth waves  $U_{H, Stokes}^{(2)}$  (Eq. (2)) for the corresponding wave heights. Notably, calculations above the still water level are conducted utilizing the linear extrapolation method (Det Norske Veritas, 2000). Away from the fluid–structure interface, the velocity profile under the flexible structure aligns quite well with the analytical predictions. A maximum  $U_H$  is observed close to the fluid–structure interface and decays exponentially as water depth increases. The distinct deviation from the theoretical solution at the fluid–structure interface will be discussed in the subsequent section. For the rigid model, due to the reduced aforementioned crest height, both the predicted and the measured velocities underneath the structure are significantly lower than those underneath the flexible one. However, here the theoretical and measured velocities differ in both magnitude and gradient with vertical distance: the theoretical prediction based

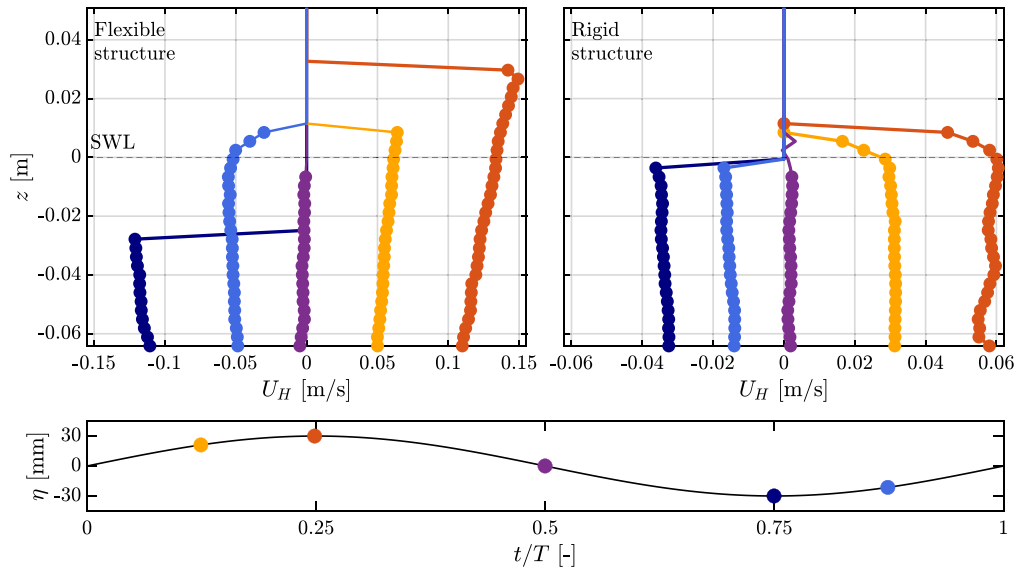


Fig. 13. Results for wave W3-2 under the flexible and rigid floating structure. Comparison of  $U_H$  at different wave phases.

on the effective wave height decrease underestimates the measured velocity underneath the rigid model by about 16%. Moreover, instead of the conventional exponential decay, the profile manifests an almost constant magnitude of velocity across the water depth. Fig. 13 presents the horizontal velocity profiles measured for W3-2, considering both flexible and rigid structures at various wave phases. The previous observations about the wave crests are also reflected across different wave phases. In comparison to the wave interacting with the flexible structure, the wave under the rigid structure experiences a 59.7% reduction in wave crest amplitude (and 60% in the maximum horizontal wave velocity underneath it, maximum of  $U_H$ ) and a 75.6% decrease in wave trough amplitude (and 77% in the maximum horizontal wave velocity underneath it, minimum of  $U_H$ ). While the velocity profiles under the flexible cover decay exponentially with water depth, the profiles under the rigid structure maintain a relatively constant velocity with  $z$ . These trends are also consistent for wave conditions W3-1. Comparisons with the two shorter waves W6-1 and W6-2 were not feasible due to measurement limitations and as such are omitted here.

### 3.3. Wave boundary layer

The boundary layer in oscillatory flows over a wall is typically confined to a thin region near the fluid–structure interface. In the case of laminar flow, the Stokes layer thickness or the viscous penetration depth is given by  $\delta_s = \sqrt{2\nu/\omega}$  (Sana and Tanaka, 2007). For the current wave conditions, this translates to a thickness of  $\delta_s = 2.9\text{--}4.2$  mm. However, due to limitations in the resolution of PIV measurements and interference from laser reflections close to the wave–structure interface, a clear indication of a wave-induced boundary layer at the interface was only observed for wave condition W3-2 at the wave crest under the flexible structure. During this specific phase of the wave, we reprocessed the velocity fields with an IW size of  $16 \times 64$  pixel and 50% overlap in order to allow for a better resolution close to the fluid–structure interface. Fig. 14 illustrates  $U_H$  at the wave crest of W3-2 in proximity to the wave-flexible structure interface.

Near the interface,  $U_H$  deviates from the theoretical free surface solution  $U_{H,Stokes}^{(2)}$ , surpassing the theoretical value before eventually reaching  $U_H = 0$  m s<sup>-1</sup> at the interface. This type of ‘overshoot’ is a common characteristic of oscillatory boundary layer near the interface (Sana and Tanaka, 2007), distinguishing them from steady boundary layers. To facilitate a meaningful comparison between the analytical model adapted from the 2nd Stokes problem  $U_H^*$  and the

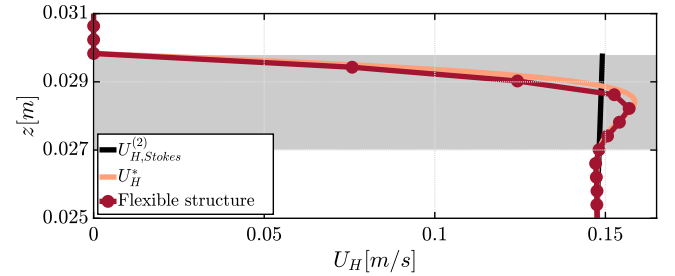


Fig. 14. WBL at the wave-structure interface of W3-2 at the wave crest. The gray shaded segment along the  $z$ -axis corresponds to  $\delta$ .

experimental data  $U_H$  (Eq. (5)), we used the measured velocity  $U_H$  at the point where it deviates from  $U_{H,Stokes}^{(2)}$ . The experimental data closely matches the theoretical solution, and the boundary layer thickness ( $\delta$ ), defined as the distance from the interface where  $U_H = 0$  m s<sup>-1</sup> to the aforementioned deviation point measures approximately  $\delta = 3$  mm (see gray shaded region in Fig. 14). While this model matches our experimental data at the wave crest of wave W3-2 well, further analysis of the wave boundary layer throughout the wave cycle is necessary to assess its applicability for 2nd order Stokes waves. Further WBL analysis with the current study is unfeasible, necessitating future studies with higher resolution and reduced reflections at the wave–structure interface to provide additional insights.

## 4. Conclusion

A study of wave and velocity characteristics underneath both a floating and a rigid structure under wave conditions in a towing tank was presented here. For the first time, we directly measured the wave velocity field induced by these structures by simultaneously conducting PIV and wave elevation measurements, providing new insights into fluid–structure interactions. The main conclusions of this work and future research are summarized below.

- The velocity profiles under the flexible structure closely match those of a 2nd order Stokes wave in intermediate water depths, with the structure tracking the propagating wave and its elevation. An exponential decay of velocity with depth was observed, accompanied by a WBL near the wave–structure interface that

shows an ‘overshoot’ effect, characteristic of oscillatory boundary layers. The thickness of the boundary layer ( $\delta$ ) aligns well with the laminar Stokes layer thickness.

- Under the rigid structure, a significant reduction in wave elevation and velocities was noted compared to the incident wave, along with deviations from the anticipated exponential velocity decay, instead exhibiting a nearly constant velocity value with depth.
- Additional wave probe measurements showed that longer wavelengths ( $\lambda = 3$  m) maintained consistent elevation along the flexible structure, while shorter wavelengths at 0.66 m displayed a considerable decrease in wave height. This behavior aligns with existing literature, attributable to the wavelength-to-characteristic-length ratio ( $\lambda/\lambda_c$ ), a crucial factor influencing floating structures’ responses. The longer the wavelength, or the higher  $\lambda/\lambda_c$  is, the gentler the curvature of the wave, less deformation of the structure, hence less attenuation. Since the wavelength of the longer wave is closer to the structure length, there is less time to interact with the structure.
- Future experiments with increased resolution and improved optical access will further examine the fluid–structure interactions observed here, focusing on WBL dynamics at shorter wavelengths. Enhanced resolution will provide deeper insight into boundary layer behaviors near flexible structures. Additionally, examining various wavelength and wave height conditions will clarify the influence of the wavelength-to-characteristic-length ratio ( $\lambda/\lambda_c$ ) on wave attenuation and boundary layer formation, contributing to more robust designs for floating structures in offshore environments.

#### CRedit authorship contribution statement

**Esra Uksul:** Writing – original draft, Visualization, Validation, Formal analysis, Data curation, Conceptualization. **Angeliki Laskari:** Writing – review & editing, Supervision, Project administration, Conceptualization. **Sebastian Schreier:** Writing – review & editing, Supervision, Project administration, Methodology, Conceptualization. **Christian Poelma:** Writing – review & editing, Supervision, Resources, Project administration, Funding acquisition, Conceptualization.

#### Declaration of competing interest

The authors declare that they have no known competing financial interests or personal relationships that could have appeared to influence the work reported in this paper.

#### References

- Bispo, I.B., Amouzadrad, P., Mohapatra, S., Guedes Soares, C., 2023. Motion analysis of a floating horizontal set of interconnected plates based on computer vision target tracking technique. In: *Advances in the Analysis and Design of Marine Structures*. pp. 153–160. <http://dx.doi.org/10.1201/9781003399759>.
- Bispo, I.B., Mohapatra, S.C., Guedes Soares, C., 2022. Numerical analysis of a moored very large floating structure composed by a set of hinged plates. *Ocean Eng.* 253 (September 2021), 110785. <http://dx.doi.org/10.1016/j.oceaneng.2022.110785>.
- Bouvy, A., 2009. Acoustic wave height measurements in a towing facility. In: *First International Conference on Advanced Model Measurement Technology for the EU Maritime Industry (AMT’09)*, Nantes, France, September 2009. pp. 310–324.
- Chen, X.J., Wu, Y., Cui, W.C., Jensen, J.J., 2006. Review of hydroelasticity theories for global response of marine structures. *Ocean Eng.* 33 (3–4), 439–457. <http://dx.doi.org/10.1016/j.oceaneng.2004.04.010>.
- Chen, X., Zhou, W., 2023. Performance evaluation of aquavoltatics in China: Retrospect and prospect. *Renew. Sustain. Energy Rev.* 173, 113109. <http://dx.doi.org/10.1016/j.rser.2022.113109>.
- Det Norske Veritas, 2000. *Environmental conditions and environmental loads*.
- Hermans, A., 2004. Interaction of free-surface waves with floating flexible strips. *J. Eng. Math.* 49, 133–147. <http://dx.doi.org/10.1023/B:ENGI.0000017477.58851.af>.
- Lorke, A., Umlauf, L., Jonas, T., Wüest, A., 2002. Dynamics of turbulence in low-speed oscillating bottom-boundary layers of stratified basins. *Environ. Fluid Mech.* 2, 291–313. <http://dx.doi.org/10.1023/A:1020450729821>.
- Mosig, J., Montiel, F., Squire, V., 2015. Comparison of viscoelastic-type models for ocean wave attenuation in ice-covered seas. *J. Geophys. Res.: Oceans* 120 (9), 6072–6090. <http://dx.doi.org/10.1002/2015JC010881>.
- Oceans of Energy, 2024. North sea 1. <https://oceansofenergy.blue/north-sea-1/>. (Accessed 24 January 2024).
- Orzech, M., Yu, J., Wang, D., Landry, B., Zuniga-Zamalloa, C., Braithwaite, E., Trubac, K., Gray, C., 2022. Laboratory measurements of surface wave propagation through ice floes in salt water. *J. Mar. Sci. Eng.* 10 (10), 1483. <http://dx.doi.org/10.3390/jmse10101483>.
- Phillips, O.M., 1977. *The Dynamics of the Upper Ocean*. Cambridge University Press.
- Rabault, J., Sutherland, G., Jensen, A., Christensen, K.H., Marchenko, A., 2019. Experiments on wave propagation in grease ice: combined wave gauges and particle image velocimetry measurements. *J. Fluid Mech.* 864, 876–898. <http://dx.doi.org/10.1017/jfm.2019.16>.
- Robinson, N., Palmer, S., 1990. A modal analysis of a rectangular plate floating on an incompressible liquid. *J. Sound Vib.* 142 (3), 453–460. [http://dx.doi.org/10.1016/0022-460X\(90\)90661-I](http://dx.doi.org/10.1016/0022-460X(90)90661-I).
- Sahu, A., Yadav, N., Sudhakar, K., 2016. Floating photovoltaic power plant: A review. *Renew. Sustain. Energy Rev.* 66, 815–824. <http://dx.doi.org/10.1016/j.rser.2016.08.051>.
- Sana, A., Tanaka, H., 2007. Full-range equation for wave boundary layer thickness. *Coast. Eng.* 54 (8), 639–642. <http://dx.doi.org/10.1016/j.coastaleng.2007.01.011>.
- Santiago, J.G., Weresley, S.T., Meinhart, C.D., Beebe, D., Adrian, R.J., 1998. A particle image velocimetry system for microfluidics. *Exp. Fluids* 25 (4), 316–319. <http://dx.doi.org/10.1007/s003480050235>.
- Schreier, S., Jacobi, G., 2021. Experimental investigation of wave interaction with a thin floating sheet. *Int. J. Offshore Polar Eng.* 31 (04), 435–444. <http://dx.doi.org/10.17736/ijope.2021.mk76>.
- Schreier, S., Jacobi, G., 2022. Measuring hydroelastic deformation of very flexible floating structures. In: *WCFS2020: Proceedings of the Second World Conference on Floating Solutions*, Rotterdam. Springer, pp. 347–371. [http://dx.doi.org/10.1007/978-981-16-2256-4\\_21](http://dx.doi.org/10.1007/978-981-16-2256-4_21).
- Squire, V.A., 2007. Of ocean waves and sea-ice revisited. *Cold Reg. Sci. & Technol.* 49 (2), 110–133.
- Sree, D.K., Law, A.W.K., Shen, H.H., 2017. An experimental study on the interactions between surface waves and floating viscoelastic covers. *Wave Motion* 70, 195–208. <http://dx.doi.org/10.1016/j.wavemoti.2016.08.003>.
- Sree, D., Law, A.W.K., Shen, H.H., 2018. An experimental study on gravity waves through a floating viscoelastic cover. *Cold Reg. Sci. & Technol.* 155, 289–299. <http://dx.doi.org/10.1016/j.coldregions.2018.08.013>.
- Stokes, G., 1880. On the theories of the internal friction of fluids in motion, and of the equilibrium and motion of elastic solids. *Trans. Camb. Phil. Soc.* 8.
- Sutherland, G., Halsne, T., Rabault, J., Jensen, A., 2017. The attenuation of monochromatic surface waves due to the presence of an inextensible cover. *Wave Motion* 68, 88–96. <http://dx.doi.org/10.1016/j.wavemoti.2016.09.004>.
- Suzuki, H., Riggs, H., Fujikubo, M., Shugar, T., Seto, H., Yasuzawa, Y., Bhattacharya, B., Hudson, D., Shin, H., 2007. Very large floating structures. In: *International Conference on Offshore Mechanics and Arctic Engineering*. Vol. 42681, pp. 597–608. <http://dx.doi.org/10.1115/OMAE2007-29758>.
- Wadhams, P., Squire, V.A., Goodman, D.J., Cowan, A.M., Moore, S.C., 1988. The attenuation rates of ocean waves in the marginal ice zone. *J. Geophys. Res.: Oceans* 93 (C6), 6799–6818. <http://dx.doi.org/10.1029/JC093iC06p06799>.
- Wang, J., Koley, S.S., Katz, J., 2020. On the interaction of a compliant wall with a turbulent boundary layer. *J. Fluid Mech.* 899, A20. <http://dx.doi.org/10.1017/jfm.2020.446>.
- Wang, R., Shen, H.H., 2010. Gravity waves propagating into an ice-covered ocean: A viscoelastic model. *J. Geophys. Res.: Oceans* 115 (C6), <http://dx.doi.org/10.1029/2009JC005591>.
- Wang, C., Tay, Z., 2011. Very large floating structures: applications, research and development. *Procedia Eng.* 14, 62–72. <http://dx.doi.org/10.1016/j.proeng.2011.07.007>.
- Westerweel, J., 1997. Fundamentals of digital particle image velocimetry. *Meas. Sci. Technol.* 8 (12), 1379. <http://dx.doi.org/10.1088/0957-0233/8/12/002>.
- Windt, C., Davidson, J., Schmitt, P., Ringwood, J., 2019. On the assessment of numerical wave makers in CFD simulations. *J. Mar. Sci. Eng.* 7 (2), 47. <http://dx.doi.org/10.3390/jmse7020047>.
- Zhang, M., Schreier, S., 2022. Review of wave interaction with continuous flexible floating structures. *Ocean Eng.* 264, 112404. <http://dx.doi.org/10.1016/j.oceaneng.2022.112404>.